International Journal of Hydrogen Energy 58 (2024) 863–871

Contents lists available at ScienceDirect

International Journal of Hydrogen Energy

journal homepage: www.elsevier.com/locate/he

Electron bipolarons at the $DMASnBr_3$–water interface: Effect on the photocatalytic hydrogen production

Damiano Ricciarelli [a,b], Edoardo Mosconi [a], Julia Wiktor [c], Lorenzo Malavasi [d], Francesco Ambrosio [e,a,*], Filippo De Angelis [a,f,g,h,**]

[a] Computational Laboratory for Hybrid/Organic Photovoltaics (CLHYO), Istituto CNR di Scienze e Tecnologie Chimiche "Giulio Natta" (CNR-SCITEC), Via Elce di Sotto 8, Perugia, 06123, Italy
[b] National Research Council of Italy, Institute for Microelectronics and Microsystems (IMM-CNR), VIII Strada 5, Catania, 95121, Italy
[c] Department of Physics, Chalmers University of Technology, SE-412 96, Gothenburg, Sweden
[d] Department of Chemistry and INSTM, Università degli Studi di Pavia, Pavia, 27100, Italy
[e] Dipartimento di Scienze, Università degli Studi della Basilicata, Viale dell'Ateneo Lucano, 10, Potenza, 85100, Italy
[f] Department of Chemistry, Biology and Biotechnology and INSTM, University of Perugia, Via Elce di Sotto 8, Perugia, 06123, Italy
[g] Chemistry Department, College of Science, King Saud University, Riyadh, 11451, Kingdom of Saudi Arabia
[h] SKKU Institute of Energy Science and Technology (SIEST), Sungkyunkwan University, Suwon, 440-746, Republic of Korea

ARTICLE INFO

Keywords:
Water-stable metal halide perovskites
Photocatalysis
pH-dependent surface chemistry
Small electron bipolarons
Ab initio molecular dynamics
Energy levels alignment

ABSTRACT

In this article, we report on advanced molecular dynamics simulations of the atomistic $DMASnBr_3$–water interface, which, coupled with a grand-canonical formulation of adsorbates and defects, elucidate the surface chemistry and reactivity of this novel water-stable perovskite and highlight the role of small electron bipolarons in photocatalytic hydrogen production. We find that the extremely acidic nature of the surface Br atoms does not allow for significant adsorption of protons at the interface under charge-neutral conditions. However, when electrons are accumulated on the surface, the formation of a small electron bipolaron in the form of a Sn-Sn dimer provides the required electron localization to drive adsorption of H, which is assimilated on surface Sn atoms as hydride. Finally, we estimate a favourable alignment between the bipolaron energy level and the H^+/H_2 redox level, which suggests the occurrence of a feasible route for hydrogen evolution, bypassing the common reaction mechanism.

1. Introduction

Photocatalytic water splitting at the semiconductor–water interface may support the production of clean fuel by mimicking natural processes occurring in photosynthesis [1–12]. However, notwithstanding the large efforts deployed in the last decade [13–18], an ideal photocatalyst has not been found yet. In fact, a material should meet a vast number of requirements to be a candidate photocatalyst. Its band gap E_g should be comprised between 1.23 and 3 eV, in order to straddle the hydrogen reduction and the water oxidation redox levels in water, while being able to absorb the largest fraction of the visible spectrum [4,6]. A long lifetime and high mobility of the charge carriers is also desirable [19–21], along with a strong defect tolerance [22,23]. Moreover, the valence (VB) and conduction band (CB) edges should be properly aligned with respect to the redox levels of liquid water, to ensure that charge-transfer processes at the heterogeneous interface are thermodynamically favourable [24–28]. Finally, to avoid or minimize the addition of protective layers [29,30] and/or expansive co-catalysts [31], an excellent photocatalyst should be stable in aqueous environment and dissociate water on its surface [26,27,32,33].

The extensive search for the optimal photocatalyst, while encompassing a plethora of innovative materials including e.g. nanostructured [34,35], 2D [36,37], and magnetic materials [38], has for long excluded the most intriguing class of novel semiconductors, metal halide perovskites (MHPs), which are easily synthesized and display opto-electronic properties rivalling those of state-of-the-art semiconductors [39–46]. Besides, MHPs are generally defect tolerant [47–49] and the band gap and the band edges can be easily tuned by varying the composition in the ABX_3 formula, with different inorganic or inorganic A-site cations (e.g. Cs^+ and $CH_3NH_3^+$), halides (I, Br, Cl) and metals (Pb, Sn, Ge). Such a flexibility permits to easily attain, via material design, the alignment with the redox potentials in aqueous solution for the desired reactions [50,51].

* Corresponding author at: Dipartimento di Scienze, Università degli Studi della Basilicata, Viale dell'Ateneo Lucano, 10, Potenza, 85100, Italy.
** Corresponding author at: Department of Chemistry, Biology and Biotechnology and INSTM, University of Perugia, Via Elce di Sotto 8, Perugia, 06123, Italy.
E-mail addresses: francesco.ambrosio@unibas.it (F. Ambrosio), filippo@thch.unipg.it (F. De Angelis).

https://doi.org/10.1016/j.ijhydene.2024.01.268
Received 8 September 2023; Received in revised form 17 January 2024; Accepted 21 January 2024
Available online 30 January 2024

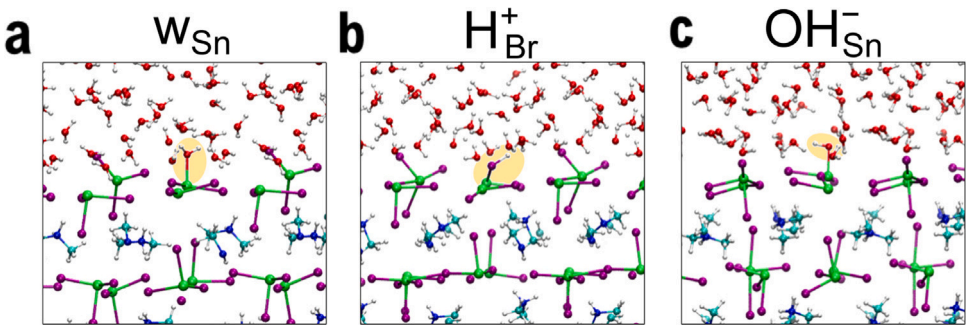

Fig. 1. Stick&ball representation (side-view) of a structural configuration of (a) an adsorbed H_2O molecule, (b) an adsorbed H^+, (c) an adsorbed OH^- at the $DMASnBr_3$(001)–water interface. Sn atoms in green, Br in purple, O in red, and H in white. (For interpretation of the references to colour in this figure legend, the reader is referred to the web version of this article.)

Two main drawbacks have hitherto hindered the efforts to introduce MHPs to photocatalysis: (i) their poor stability upon moisture and water exposure [52–55], and (ii) the large performance and stability gap between MHPs containing lead, which is toxic, and more environmental-friendly lead-free materials [56–63]. For these reasons, only in the last years, MHPs have emerged in heterogeneous photocatalysis as a possible alternative to traditional semiconductors. The first attempts to employ MHPs in photocatalytic H_2 production have been conducted either immersing the material in highly concentrated halogen acid solutions, to limit material degradation, which is usually initiated by halogen loss [47,64], or protecting the photocatalyst with water-resistant overlayers/encapsulation [51,65,66]. Nevertheless, these strategies, allowing for a proper evaluation of MHPs activity, reduce the feasibility of related devices.

Very recently, encouraging results have been obtained for Bi, Ge, and Sn perovskites possessing both significant water stability and good photocatalytic properties [67–72]. In particular, dimethylammonium tin bromide ($DMASnBr_3$) with its suitable band gap, 2.85 eV [69,73], and its band edges well positioned with respect to the redox levels of liquid, has proved to be particularly promising with measured rates of hydrogen production exceeding 1700 μmol g^{-1} h^{-1} in composites with g-C_3N_4 [69,74]. In this context, it has been established that strong electron localization associated with bipolaron formation is recurrent in tin halide perovskites (THPs) with binding energies correlated with the energy level of the CB [59,75,76]. Furthermore, bipolaron formation at the surface is predicted to be key in the hydrogen evolution reaction at the surface of THPs [76]. However, an in-depth comprehension of the surface chemistry is still lacking [77]. In fact, while the study of atomistic interfaces has unveiled the reason beyond the unprecedented water stability shown by $DMASnBr_3$ [78], the acid–base chemistry, which is fundamental in assessing the potential photocatalytic activity of candidate semiconductors [27], has not been analysed yet. Furthermore, even though the formation of electron bipolarons has been demonstrated for the bulk material and bare surfaces [75,76], a characterization of the electronic structure and associated energy levels on the more realistic interface model is mandatory to attain a more accurate depiction of the electron transfer processes possibly occurring in photocatalytic H_2 production.

In this article, we study the atomistic $DMASnBr_3$–water interface at room temperature via *ab initio* molecular dynamics (MD) simulations, which are employed to calculate free energies within a grand canonical formulation of adsorbates and defects at the heterogeneous interface. The achieved results provide fundamental insights into the surface chemistry and reactivity of this material and expand the recent but growing literature of polaronic effects in heterogeneous photocatalysis. We first study the pH-dependent surface chemistry of the $DMASnBr_3$–water interface in absence of photogenerated charges and discover that the perovskite surface is decidedly inert with protons being hardly adsorbed in a wide range of pH values. However, small electron bipolarons occurring via the formation of a Sn–Sn bond are found to provide the much-needed charge localization to induce H adsorption as surface hydride. Finally, from the alignment of the band edges and the polaronic energy level of $DMASnBr_3$ with the redox levels of liquid water, we evince a favourable energetics towards photocatalytic hydrogen production, within a reaction path alternative to the traditional mechanism.

2. Computational details

We carry out DFT Born–Oppenheimer molecular dynamics (MD) simulations of the atomistic interface between liquid water and $DMASnBr_3$ with the CP2K suite of programs [79]. Simulations are carried out in the NVT ensemble. The target temperature, controlled with a Nose–Hoover thermostat [80,81], is set at 350 K, in order to achieve liquid-like behaviour and to approximately take into account nuclear quantum motion [82]. A time-step of 0.48 fs is employed to properly sample the fast stretching modes of liquid water. Production runs of 8–10 ps are preceded by an equilibration run of 2 ps. Simulations are performed with the rVV10 functional [83,84], to correctly include non-local electron correlation. Goedecker–Teter–Hutter pseudopotentials are used to account for core-valence interactions [85]. We employ the MOLOPT double-ζ polarized basis sets [86] and a cut-off of 600 Ry for the expansion of the electron density in plane waves. The choice of a semilocal functional is here motivated by the benchmark carried out in a previous study, in which it has been shown that the energetics of conduction band states and of localized electrons is close to that achieved with more computationally expansive hybrid functionals [76]. We have further verified this by re-evaluating specific total-energy differences at the hybrid-DFT [87–94] level (cf. Supplementary Information).

3. Results and discussion

We first consider a neutral $DMASnBr_3$(001)–water interface. This is constructed as 2 × 2 orthorhombic supercell [a = 12.274, b = 12.071, and c = 47.500 Å with a and b corresponding to experimental values [69], cf. Figure S1 (a)]. The model includes 72 H_2O molecules, corresponding to the experimental density of liquid water [cf. Figure S1 (b)]. Such a model has been extensively characterized in a previous study [78] and features a $SnBr_2$-terminated slab, with water molecules being molecularly adsorbed on the semiconductor interface through a Sn–O bond of ~2.40 Å and only weakly interacting with surface Br sites as illustrated by the Sn–O and H–Br radial distribution functions [cf. Figure S1 (c)]. We note that the use of a $SnBr_2$-terminated slab is here motivated by the higher stability that BX_2 surfaces exhibit with respect to those featuring an AX coverage [54].

Starting from the neutral $DMASnBr_3$(001)–water interface [w_{Sn}, cf. Fig. 1(a)], we carry out molecular dynamics (MD) simulations (i) where an extra proton is added close to a surface Br atom (H^+_{Br}) [cf. Fig. 1(b)] and (ii) in which an adsorbed H_2O molecule is replaced by an hydroxyl ion (OH^-_{Sn}) [cf. Fig. 1(c)]. For H^+_{Br} we estimate an average H–Br distance

of 1.70 Å, ~0.3 Å longer than HBr bond length. A small reduction of the Sn–O bond (~0.2 Å) is observed when an adsorbed water molecule is replaced by an hydroxyl ion [cf. Fig. 1c], as a consequence of a stronger Sn–O interaction.

To evaluate the pH-dependent surface chemistry at the semiconductor–water interface, we calculate the acidity of the surface sites. To this end, we consider the adsorbed species being subject to following acid–base equilibria:

$$H^+_{Br} + H_2O(l) \rightarrow Br_{surf} + H_3O^+(aq), \tag{1}$$

$$w_{Sn} + H_2O^+(l) \rightarrow OH^-_{Sn} + H_3O^+(aq), \tag{2}$$

which represent the acidic dissociation of the adsorbed proton and water molecule, respectively. The associated acidic constants read as follows:

$$K_a(H^+_{Br}) + = \frac{[Br_{surf}][H_3O^+(aq)]}{[H^+_{Br}]}, \tag{3}$$

$$K_a(w_{Sn}) = \frac{[OH^-_{Sn}][H_3O^+(aq)]}{[w_{Sn}]}, \tag{4}$$

and are here calculated with a grand-canonical formulation of adsorbates at the interface [27,32,82,95–97], which allow to express the free-energy differences of the reactions by combining MD simulations with the thermodynamic integration method [98,99]. In particular, the acidity of an adsorbate can be expressed in terms of the difference between its deprotonation free energy and that of the aqueous hydronium cation [27,32], the latter hence acting as a reference:

$$pK_a(H^+_{Br}) = \frac{\Delta_{dp}G(H^+_{Br})}{\ln 10 \cdot k_B T} - \log c_0, \tag{5}$$

$$pK_a(w_{Sn}) = \frac{\Delta_{dp}G(w_{Sn})}{\ln 10 \cdot k_B T} - \log c_0. \tag{6}$$

In Eqs. (5) and (6), $\Delta_{dp}G(H^+_{Br})$, and $\Delta_{dp}G(H^+_{Br})$ are hence the free energy changes associated with deprotonation adsorbed proton and adsorbed water molecule, respectively, referred to that of the aqueous hydronium cation, i.e. the free energies of reactions (1) and (2). k_B is the Boltzmann's constant and c_0 is the number of water moles in 1 L of liquid water (55.5 mol/dm^3). $\Delta_{dp}G(H^+_{Br})$ and $\Delta_{dp}G(w_{Sn})$ are defined as [27,32]:

$$\Delta_{dp}G(H^+_{Br}) = \Delta_{dp}A(H^+_{Br}) - \Delta_{dp}A(H_3O^+) - \Delta_{zp}E(H^+_{Br}) + \Delta_{zp}E(H_3O^+) + \Delta V_w, \tag{7}$$

$$\Delta_{dp}G(w_{Sn}) = \Delta_{dp}A(w_{Sn}) - \Delta_{dp}A(H_3O^+) - \Delta_{zp}E(w_{Sn}) + \Delta_{zp}E(H_3O^+) + \Delta V_w. \tag{8}$$

In Eqs. (7) and (8), $\Delta_{dp}A(H^+_{Br})$, $\Delta_{dp}A(w_{Sn})$, and $\Delta_{dp}A(H_3O^+)$ are the deprotonation free energies of adsorbed proton, adsorbed water molecule, and aqueous hydronium cation, respectively. $\Delta_{dp}A(H^+_{Br})$ and $\Delta_{dp}A(w_{Sn})$ are here calculated within the Marcus approximation:

$$\Delta_{dp}A(H^+_{Br}) = \frac{\langle \Delta_{dp}E(H^+_{Br})\rangle_0 + \langle \Delta E(H^+_{Br})\rangle_1}{2}, \tag{9}$$

$$\Delta_{dp}A(w_{Sn}) = \frac{\langle \Delta_{dp}E(w_{Sn})\rangle_0 + \langle \Delta E(w_{Sn})\rangle_1}{2}, \tag{10}$$

where $\langle \Delta_{dp}E(H^+_{Br})\rangle_0$ and $\langle \Delta_{dp}E(w_{Sn})\rangle_0$ are the average vertical energies of proton detachment, while $\langle \Delta_{dp}E(H^+_{Br})\rangle_1$ and $\langle \Delta_{dp}E(w_{Sn})\rangle_1$ the average vertical proton attachment. The former are calculated from a set of 200 configurations equally spaced in time. For each configuration, we vertically remove the acidic proton and recalculate the total-energy keeping the other atoms fixed. For the latter, we add a proton close to the surface Br site and to an adsorbed hydroxyl ion, respectively. Then, we perform structural relaxations in which all atoms except the inserted proton are fixed. $\langle \Delta_{dp}E(H^+_{Br})\rangle_1$ and $\langle \Delta_{dp}E(w_{Sn})\rangle_1$ are hence computed from total-energy differences between the structural configurations with and without the proton. This procedure allows us to achieve converged results employing a set of 20 MD snapshots [32]. For $\Delta_{dp}A(H_3O^+)$, we employ the value calculated in Ref. [82]. $\Delta_{zp}E(H^+_{Br})$, $\Delta_{zp}E(w_{Sn})$, and $\Delta_{zp}E(H_3O^+)$ are the zero-point motion corrections accounting for the lack of nuclear quantum motions in our MD simulations. These contributions to the free energy are here calculated from the vibrational frequencies of the normal modes associated with the proton undergoing acidic dissociation [32,82]. Finally, ΔV_w is the difference between the electrostatic potential of liquid water in the model of bulk water and in the respective bulk component of the interface model, which is required to align the calculations to an identical reference. This term is here calculated from the alignment of the O 2*s* of water molecules in the bulk liquid and those in the bulk-like region of the interface model [25,100]. We note that electrostatic finite-size effects for periodic charged supercell, which has been estimated with a correction scheme for the formation energy of charged defects at the interface [95,101], have been found here to be minimal, because of the strong screening of the semiconductor and the water molecules. Therefore, correction terms have been not included. All the calculated quantities are listed in Table 1.

Table 1
List of the quantities (cf. text for definition) calculated to estimate free-energy differences, acidities, and band alignment reported in the main text. All values are given in eV.

Quantity	Value
$\Delta_{dp}A(H_3O^+)$	15.15 [102]
$\Delta_{dp}A(H^+_{Br})$	15.40
$\Delta_{dp}A(w_{Sn})$	16.51
$\Delta_{zp}E(H_3O^+)$	0.32 [82]
$\Delta_{zp}E(H^+_{Br})$	0.11
$\Delta_{zp}E(w_{Sn})$	0.30
ΔV_w	−0.80
ΔV_{SC}	1.40

We here estimate $pK_a(H^+_{Br}) = -7.50$ and $pK_a(H^+_{Br}) = 7.75$. Therefore, the surface Br site is a strong acid with protons being unlikely to be adsorbed on the perovskite surface under realistic pH conditions. At variance with this, the water molecule is found to increase its acidity when adsorbed on a surface Sn site from 15.74 to 7.75, slightly inferior to that previously reported for other tin-based semiconductors with a similar surface (i.e. ~5 for SnO_2). From the calculated values of pK_a, it follows that the dissociation reaction:

$$w_{Sn} + Br_{surf} \rightarrow OH^-_{Sn} + H^+_{Br} \tag{11}$$

entails a free energy as large as 1.06 eV, again in accord with the low reactivity of this surface [76,78].

Next, we construct a logarithmic concentration diagram of adsorbed species from the calculated pK_as, in analogy to those usually employed to visualize the concentration of weak acids in aqueous solution. To this end, we rearrange Eqs. (3) and (4) to explicit the pH-dependence of the adsorbed species:

$$\frac{[Br_{surf}]}{[H^+_{Br}]} = \frac{K_a(H^+_{Br}) +}{[H_30^+(aq)]} = \frac{10^{-pK_a(H^+_{Br})}}{10^{-pH}}, \tag{12}$$

$$\frac{[OH^-_{Sn}]}{[w_{Sn}]} = \frac{K_a(w_{Sn})}{[H_3O^+(aq)]} = \frac{10^{-pK_a(w_{Sn})}}{10^{-pH}}, \tag{13}$$

and we impose:

$$c_{Br} = [H^+_{Br}] + [Br_{surf}], \tag{14}$$

$$c_{Sn} = w_{Sn} + [OH^-_{Sn}], \tag{15}$$

i.e. total concentration of an acidic species and of its the conjugated base is given by the surface site concentration (expressed in mol/dm^2).

The concentration diagram for all the adsorbed species at the $DMASnBr_3(001)$–water interface is presented in Fig. 2. We note that

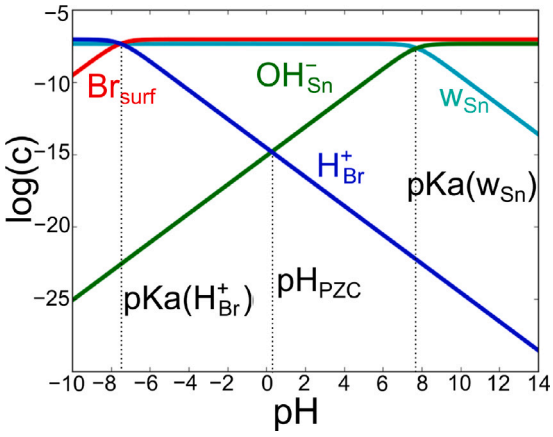

Fig. 2. pH-dependent diagram of surface coverage of at the $DMASnBr_3(001)$–water interface. Concentrations are given in mol/dm^2.

hydroxyl anions, initiating the water oxidation reaction within the faster alkaline mechanism, are abundant on the perovskite surface already in a mildly basic solution. In stark contrast, protons, the source of photoreduced hydrogen, are not likely to be found attached on the perovskite surface under the operative pH conditions of a heterogeneous photocatalytic system. We also pinpoint that the intersection between the pH-dependent concentrations of H^+_{Br} and $OH_{Sn}{}^-$ define the pH at which the interface is charge-neutral, i.e. the so-called pH point of zero charge pH_{PZC}. This is found to occur at 0.30, with concentration of ionic species being nevertheless negligible.

Since H adsorption on the surface is considered to be fundamental for the hydrogen evolution reaction on semiconductors [103,104], our results indicate the need of an alternative mechanism to justify the experimentally observed H_2 production. Therefore, we verify if the physical picture changes under photo-charging conditions, i.e. when photo-generated electrons are assimilated on the surface. In particular, we aim at verifying whether H adsorption on available surface Sn sites could be possible. To this end, we employ a simplified model in which the H defect is adsorbed on the bare $DMASnBr_3(001)$ surface, either on a surface Br or on a surface Sn atom. We consider three different charge states for the H defect: positive (+1), neutral (0), and (−1) negative, and for each of them, we relax the structures and calculate the total-energy difference $\Delta E[H]^q$ (Cf. Supplementary Information for details of the calculations):

$$\Delta E[H]^q = E[H_{Sn}]^q - E[H_{Br}]^q, \tag{16}$$

where $E[H_{Sn}]^q$ and $E[H_{Br}]^q$ are the total energy of the slab bearing the H defect on surface Br and Sn, respectively.

From Fig. 3(a), $\Delta E[H]^{+1} = 0.28$ eV indicates that a surface Sn is even more acidic than Br, in line with the cationic nature of the metal in MHPs. However, this is completely reversed when adding electrons to the system, as we compute for both $\Delta E[H]^0$ and $\Delta E[H]^{-1}$ negative values, −0.26 and −1.03 eV, respectively. We hence analyse the electronic densities of states (DOS) of the studied slabs at $q = -1$. The absence of any in-gap state for H_{Br} [3(b)] means that the injected electrons are assimilated in the conduction band. In contrast, a localized state well below the conduction band appears in the DOS when H is adsorbed on a surface Sn site [3(c)]. Such a state is associated with charge localization on the Sn bearing the H and is extended up to the four neighbouring Br atoms, as highlighted by the projected density of state and illustrated from the isodensity plot of the highest occupied molecular orbital (HOMO) of the system [Fig. 3(c) and inset]. From the analysis of the centres of the maximally localized Wannier functions [105], which yield a real-space representation of the electron localization, we evince that an electron pair is actually on the adsorbed H (cf. Figure S2), i.e. a surface hydride has been formed.

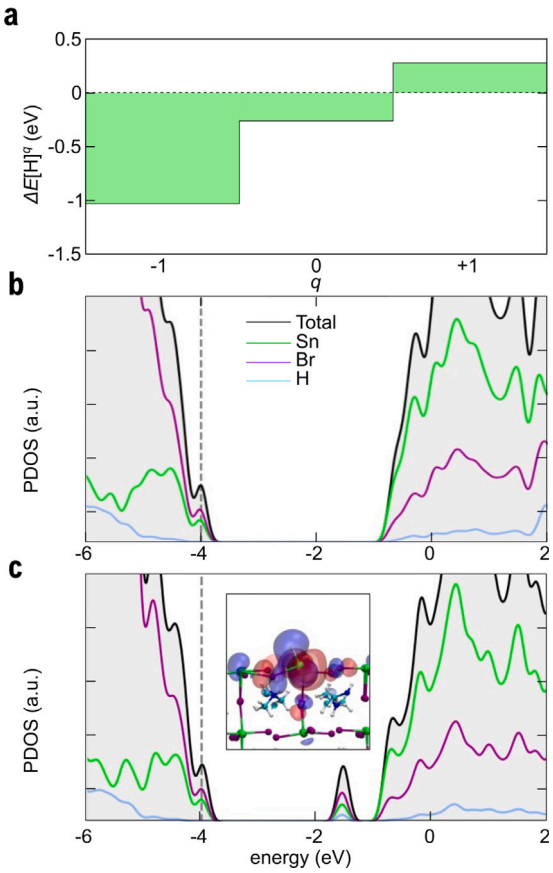

Fig. 3. (a) $\Delta E[H]^q$ (cf. main text) for different values of q. Total and partial electronic density of states for the $DMASnBr_3$ (001) slab with a H defect in the charge state $q = -1$ on (c) a surface Br and (c) a surface Sn (inset for the isodensity representation of the localized in-gap electronic state). The energy level of the highest occupied molecular orbital (HOMO) of the pristine neutral slab is indicated by a dashed vertical line.

The activity of surface sites should not change under photo-charging conditions if the photo-generated charges are delocalized/semilocalized [106]. As a matter of fact, we verify that the interface composition is barely affected when the MD simulation of the system is carried out with two extra electrons assimilated in the CB of the perovskite (cf. Figure S3). Therefore, in absence of any prior surface localization of electrons, hydride formation remains unlikely. However, the polaronic nature of charge carriers at the water–semiconductor interface can influence the acidity and reactivity of surface sites, e.g. TiO_2 [107,108], WO_3 [109], $BiVO_4$ [106,110–113], as well as the energy levels alignment [114]. On this subject, it has been recently demonstrated that electrons in THPs localize as small bipolarons, upon formation of a Sn-Sn bond with concomitant displacement of a lattice iodine [75]. Moreover, a reaction mechanism involving bipolaron formation has been recently proposed to justify the conspicuous photocatalytic activity of $DMASnBr_3$ [76].

In order to investigate the occurrence of such a localization mechanism at a realistic perovskite/water interface, we here construct a structural model in which we initially enforce the dimer formed by two surface tin atoms. Then, we carry out a 8-ps MD simulation of this system with two extra electrons. We observe that the dimeric structure, with an average bond length of 3.05 Å, and the associated electron localization [cf. Fig. 4(a)] are retained throughout the MD simulation, as evidenced by the time evolution of the energy of the highest occupied molecular orbital (HOMO) in Fig. 4(b) and of the bond length (cf. Figure S4). We also analyse how water molecules at

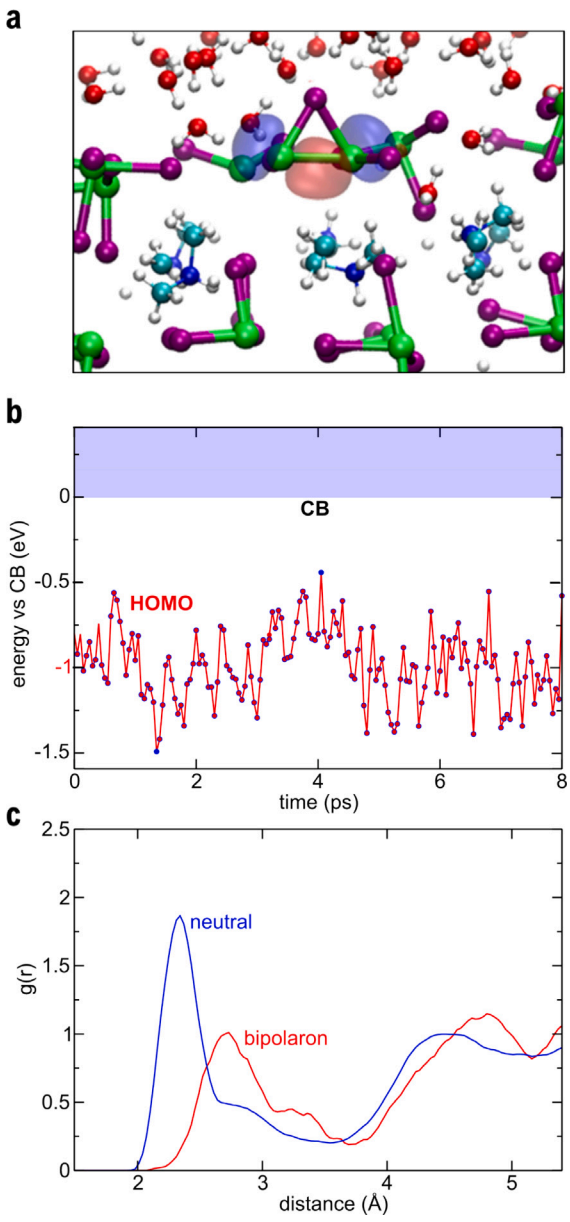

Fig. 4. (a) Isodensity representation and (b) time evolution of the HOMO for the electron bipolaron at the $DMASnBr_3$/water interface. Shaded area for the conduction band. Energies are referred with respect to the CB edge of $DMASnBr_3$ (c) Comparison between the Sn-O RDFs for tin atoms forming the dimer (solid line) and other tin atoms (dashed line) at the interface.

the interface interact with tin atoms forming the dimer. To this end, we compare the Sn-O RDF for the tin atoms belonging to the bipolaron with that achieved for the regular surface Sn atoms. The data, Fig. 4(c), reveal a noticeable change in the solvation of dimeric Sn atoms: the average Sn-O distance in the first solvation shell is increased from to 2.40 to ~2.80 Å as water molecules rearrange to point their hydrogen atoms towards the electron-rich moiety. This suggest a clear variation in the reactivity for the Sn atoms forming the dimer, which could be captured only with simulations explicitly including water molecules.

To further verify our reasoning, we place a single proton on top of a Sn atom forming the bipolaron and we let the system evolve via MD. We observe that the Sn-Sn is immediately broken while the adsorbed proton is reduced to a surface hydride with an average bond length of 1.75 Å. Therefore, the bipolaron effectively acts as an "hotspot" for the otherwise implausible H adsorption. We also denote a substantial interaction between the negatively charged hydride and a surrounding water molecule pointing one of its hydrogen atoms towards it, with an average distance of ~1.80 Å (cf. Figure S5). This, combined with the poor alkalinity of neighbouring surface sites, suggests that the H_2 production may proceed via a Heyrovsky-like step [115], i.e. direct proton transfer from condensed-phase water molecule.

Finally, we refer the band edges of $DMASnBr_3$ to the energy levels of liquid water via a computational standard hydrogen electrode (μ_{SHE}) [82,116], defined by the reduction of the hydronium ion to gaseous hydrogen in aqueous solution [82,102], through the alignment of the plane-averaged electrostatic potential [24–26,100,117]. Our simulation of a water–semiconductor interface corresponding to pH_{PZC} allow us to define the position of the valence band edge at PZC [25]:

$$\epsilon_V^{SHE}(PZC) = \epsilon_V^{theory} - \mu_{SHE} - \Delta V_{SC} + \Delta V_w, \tag{17}$$

where ϵ_V^{theory} is the calculated valence band edge of the bulk semiconductor, $\Delta V_{SC} = V_{SC}(bulk) - V_{SC}(int)$ the potential shift for the semiconductor at the interface, calculated from differences in the average electrostatic potentials in the bulk and at the interface. Analogously, the alignment of the conduction band edge is achieved as follows:

$$\epsilon_C^{SHE}(PZC) = \epsilon_V^{SHE} + E_g^{theory}, \tag{18}$$

i.e. by adding the calculated band gap to the valence band edge position. A schematic representation of the alignment scheme is provided in Supplementary Information, Figure S6. The band gap and band edges of $DMASnBr_3$ are taken from advanced electronic-structure calculations of Ref. [69], μ_{SHE} from Ref. [102], while ΔV_{SC} is computed in this study (cf. Table 1). We also include in the energy diagram (i) the H^+/H_2 redox potential and (ii) the OH^*/H_2O and OH^*/OH^- reduction potentials, since dehydrogenation of the water molecule and oxidation of the hydroxyl ion represent the first step of the water oxidation reaction under acidic and alkaline conditions, respectively. In particular, for H^+/H_2 and OH^*/OH^-, we adopt the values calculated in the solution [82,102] while the OH^*/H_2O redox level is inferred from a two-step process involving sequentially the deprotonation of the adsorbed molecule (calculated here) and the oxidation of the hydroxyl ion (from Ref. [82]). Finally, in order to adjust the band edges (aligned at pH_{PZC}) and the standard redox levels (evaluated at pH = 0) to their values at pH = 7, we assume Nernstian behaviour for both, i.e. a shift of the levels towards the vacuum level with a rate of 0.059 eV per pH unit [25,27,32].

The calculated band alignment is reported in Fig. 5, with the VB (CB) edge of $DMASnBr_3$ being placed 1.25 (1.60) eV below (above) the SHE level, within 0.2 eV with that achieved in Ref. [69], in which explicit semiconductor–water interactions were not included, an additional evidence of the weak MHP–water interactions [78,118,119]. This implies that initiation of the water oxidation reaction via the acidic mechanism, involving dehydrogenation of a water molecule, is subject to a sizable energy barrier of 0.68 eV, since the redox level lies 1.93 eV above the SHE. However, we find that the OH^-/OH^* level is almost resonant with the VB of the perovskite. This, in conjunction with the large fraction of hydroxyl anions adsorbed on the surface at pH > 7 [cf. Fig. 1(d)], points out that water oxidation should be more efficient in alkaline conditions, in accord with the experiment [69]. We note that, while most studies on MHPs have been dedicated to photocatodes, these findings suggest that exploring their possible application of as photoanodes might deserve a dedicated focus. The CB of $DMASnBr_3$ lies 1.17 eV above the H^+/H_2 redox potential and such an alignment, while energetically favourable, is kinetically undesirable for charge transfer, as its rate features an inverse exponential dependence on the energy difference between initial and final states [120]. Furthermore, the extreme acidity of surface Br sites corresponds to negligible adsorption of protons in a large pH range, thus essentially ruling out a

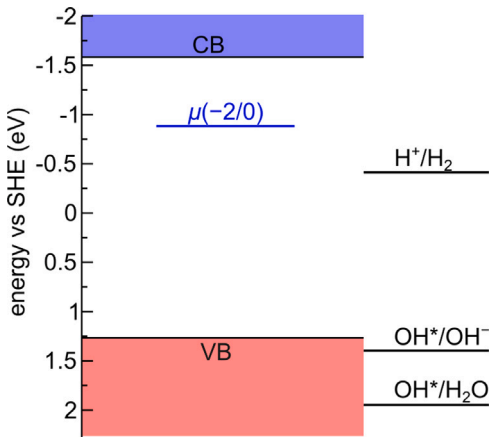

Fig. 5. VB and CB of $DMASnBr_3$ aligned with respect to the SHE at pH = 7. The alignment also includes the relevant water redox potentials and the $\mu(-2/0)$ charge transition level associated with the electron bipolaron at the $DMASnBr_3$/water interface (cf. main text).

traditional reaction mechanism. However, as small bipolarons occur at the interface, we need to evaluate also the related energy level.

To this end, we calculate the charge transition level associated with the electron bipolaron, which is defined as [106]:

$$\mu(-2/0) = \frac{G^{-2}[\text{bipol}] - G[\text{ref}]}{2} - \epsilon_V, \tag{19}$$

where $G^{-2}[\text{bipol}]$ is the free energy of the bipolaron at the perovskite/water interface, $G[\text{ref}]$ the free energy of the pristine interface model, and ϵ_V the valence band edge of $DMASnBr_3$. The free energy difference is again calculated as a thermodynamic integral of vertical energy gaps. In particular, within the Marcus approximation:

$$G^{-2}[\text{bipol}] - G[\text{ref}] = \frac{\langle \Delta E \rangle_0 + \langle \Delta E \rangle_1}{2}, \tag{20}$$

where $\langle \Delta E \rangle_0$ corresponds to the energy of vertical injection of two electrons on the pristine systems, while $\langle \Delta E \rangle_1$ to the energy of vertical removal of two electrons from the interface model bearing the bipolaron. Combining Eqs. (19) and (20), we obtain:

$$\mu(-2/0) = \frac{\langle \Delta E \rangle_0 + \langle \Delta E \rangle_1}{4} - \epsilon_V. \tag{21}$$

Consequently, the binding energy, referred with respect to the conduction band edge of the perovskite, is defined as:

$$E_b = \epsilon_C - \mu(-2/0). \tag{22}$$

We here estimate a binding energy of 0.70 eV, a value larger than those previously calculated for the bulk material (0.36 eV [75]) and the bare surface (up to 0.6 eV [76]). Such a result is in accord with the tendency, shown by liquid water, of stabilizing polaronic localization at the interface [106]. By placing $\mu(-2/0)$ on the energy diagram of Fig. 5, we observe that the bipolaron energy level lies only 0.47 eV above the H^+/H_2 redox level, which paves a more viable route towards hydrogen reduction, if compared to direct electron transfer from the CB of $DMASnBr_3$. Therefore, our analysis highlights the clear role of electron bipolarons at the water–perovskite interface in promoting the photocatalytic H_2 production. However, it should be noted that, due to the robust stability of the bipolaron, the actual reaction mechanism may still involve steps generating an overpotential [76].

4. Conclusions

In conclusion, we performed first-principles MD simulations of the atomistic $DMASnBr_3$–water interface, which, in conjunction with a grand-canonical formulation of adsorbates and defects, enabled a comprehensive description of the pH-dependent interface composition with particular focus on the negligible concentration of adsorbed protons within the pH range of an actual photocatalytic device. While such an inert surface chemistry would inhibit photocatalytic hydrogen production, our computational investigation of small electron bipolarons forming at the surface upon capture of photogenerated charges illustrated their dual beneficial role on photocatalysis. In fact, from one side, they provide the required charge localization for H adsorption in the form of surface hydride. On the other, the polaronic charge transition level was found to be favourably aligned with respect to the hydrogen reduction potential. The present results represent further proof that small polarons at the heterogeneous interface may be key to boost photocatalytic activity, sidestepping conventional reaction mechanisms.

Associated content

Benchmark of the employed rVV10 functional vs. hybrid DFT, visual representation of the centres of Wannier functions for the hydride adsorbed on the $DMASnBr_3$(001) surface, time evolution of the Sn-Sn bond length for the electron bipolaron, representative structural configuration of the hydride at the heterogeneous interface. Input files and snapshots of MD simulations are available at https://github.com/fra85uni/dmasbr3-bipolaron.

CRediT authorship contribution statement

Damiano Ricciarelli: Writing – original draft, Investigation, Formal analysis, Visualization. **Edoardo Mosconi:** Software, Methodology, Investigation. **Julia Wiktor:** Conceptualization, Writing – review & editing, Methodology. **Lorenzo Malavasi:** Conceptualization, Writing – review & editing. **Francesco Ambrosio:** Conceptualization, Methodology, Formal analysis, Writing – original draft, Investigation, Visualization. **Filippo De Angelis:** Supervision, Writing – review & editing, Resources, Funding acquisition, Conceptualization.

Declaration of competing interest

The authors declare that they have no known competing financial interests or personal relationships that could have appeared to influence the work reported in this paper.

Acknowledgements

This work has been funded by the European Union project PERTPV under grant agreement no. 763977. F.D.A. acknowledges financial support from MIUR and Università degli Studi di Perugia through the program “Dipartimenti di Eccellenza 2018-2022” (Grant AMIS). F.D.A also acknowledges funds by the European Union - NextGenerationEU under the Italian Ministry of University and Research (MUR) National Innovation Ecosystem grant ECS00000041 - VITALITY. J. W. acknowledges funding from “Genie”, “Area of Advance - Materials Science” at Chalmers University of Technology, Sweden, and the Swedish Research Council (2019-03993). F.A. thankfully acknowledges the PRIN2022-PNRR project DELPHI (project code: P2022W9773).

Appendix A. Supplementary data

Supplementary material related to this article can be found online at https://doi.org/10.1016/j.ijhydene.2024.01.268.

References

[1] Fujishima A, Honda K. Electrochemical photolysis of water at a semiconductor electrode. Nature 1972;238:37.

[2] Tachibana Y, Vayssieres L, Durrant JR. Artificial photosynthesis for solar water-splitting. Nat Photon 2012;6:511.

[3] Ahmad H, Kamarudin S, Minggu L, Kassim M. Hydrogen from photo-catalytic water splitting process: A review. Renew Sustain Energy Rev 2015;43:599.

[4] Kudo A, Miseki Y. Heterogeneous photocatalyst materials for water splitting. Chem Soc Rev 2009;38:253.

[5] Zou X, Zhang Y. Noble metal-free hydrogen evolution catalysts for water splitting. Chem Soc Rev 2015;44:5148.

[6] Maeda K, Domen K. Photocatalytic water splitting: Recent progress and future challenges. J Phys Chem Lett 2010;1:2655.

[7] Hisatomi T, Kubota J, Domen K. Recent advances in semiconductors for photocatalytic and photoelectrochemical water splitting. Chem Soc Rev 2014;43:7520.

[8] Osterloh FE, Parkinson BA. Recent developments in solar water-splitting photocatalysis. MRS Bull 2011;36:17.

[9] Moniruddin M, Ilyassov B, Zhao X, Smith E, Serikov T, Ibrayev N, Asmatulu R, Nuraje N. Recent progress on perovskite materials in photovoltaic and water splitting applications. Mater Today Energy 2018;7:246.

[10] Walter MG, Warren EL, McKone JR, Boettcher SW, Mi Q, Santori EA, Lewis NS. Solar water splitting cells. Chem Rev 2010;110:6446.

[11] Moniz SJ, Shevlin SA, Martin DJ, Guo Z-X, Tang J. Visible-light driven heterojunction photocatalysts for water splitting – a critical review. Energy Environ Sci 2015;8:731.

[12] Bahnemann D, Robertson P, Wang C, Choi W, Daly H, Danish M, de Lasa H, Escobedo S, Hardacre C, Jeon TH, Kim B, Kisch H, Li W, Long M, Muneer M, Skillen N, Zhang J. 2023 Roadmap on photocatalytic water splitting. J Phys Energy 2023;5(1):012004.

[13] Liu J, Liu Y, Liu N, Han Y, Zhang X, Huang H, Lifshitz Y, Lee S-T, Zhong J, Kang Z. Metal-free efficient photocatalyst for stable visible water splitting via a two-electron pathway. Science 2015;347:970.

[14] Luo J, Im J-H, Mayer MT, Schreier M, Nazeeruddin MK, Park N-G, Tilley SD, Fan HJ, Grätzel M. Water photolysis at 12.3% efficiency via perovskite photovoltaics and earth-abundant catalysts. Science 2014;345:1593.

[15] Kim TW, Choi K-S. Nanoporous $BiVO_4$ photoanodes with dual-layer oxygen evolution catalysts for solar water splitting. Science 2014;343:990.

[16] Liao L. Efficient solar water-splitting using a nanocrystalline CoO photocatalyst. Nat Nanotechnol 2014;9:69.

[17] Pham TA, Ping Y, Galli G. Modelling heterogeneous interfaces for solar water splitting. Nature Mater 2017;16(4):401–8.

[18] Barry E, Burns R, Chen W, De Hoe GX, De Oca JMM, de Pablo JJ, Dombrowski J, Elam JW, Felts AM, Galli G, Hack J, He Q, He X, Hoenig E, Iscen A, Kash B, Kung HH, Lewis NHC, Liu C, Ma X, Mane A, Martinson ABF, Mulfort KL, Murphy J, Mølhave K, Nealey P, Qiao Y, Rozyyev V, Schatz GC, Sibener SJ, Talapin D, Tiede DM, Tirrell MV, Tokmakoff A, Voth GA, Wang Z, Ye Z, Yesibolati M, Zaluzec NJ, Darling SB. Advanced materials for energy-water systems: The central role of water/solid interfaces in adsorption, reactivity, and transport. Chem Rev 2021;121(15):9450–501.

[19] Leng W, Barnes PR, Juozapavicius M, O'Regan BC, Durrant JR. Electron diffusion length in mesoporous nanocrystalline TiO_2 photoelectrodes during water oxidation. J Phys Chem Lett 2010;1:967.

[20] Li X, Dai Y, Li M, Wei W, Huang B. Stable Si-based pentagonal monolayers: high carrier mobilities and applications in photocatalytic water splitting. J Mater Chem A 2015;3:24055.

[21] Fumanal M, Ortega-Guerrero A, Jablonka KM, Smit B, Tavernelli I. Charge separation and charge carrier mobility in photocatalytic metal-organic frameworks. Adv Funct Mater 2020;30(49):2003792.

[22] Scheuermann AG, Lawrence JP, Kemp KW, Ito T, Walsh A, Chidsey CE, Hurley PK, McIntyre PC. Design principles for maximizing photovoltage in metal-oxide-protected water-splitting photoanodes. Nature Mater 2016;15:99.

[23] Pastor E, Sachs M, Selim S, Durrant JR, Bakulin AA, Walsh A. Electronic defects in metal oxide photocatalysts. Nat Rev Mater 2022;7(7):503–21.

[24] Wu Y, Chan MKY, Ceder G. Prediction of semiconductor band edge positions in aqueous environments from first principles. Phys Rev B 2011;83:235301.

[25] Guo Z, Ambrosio F, Chen W, Gono P, Pasquarello A. Alignment of Redox levels at semiconductor–water interfaces. Chem Mater 2018;30(1):94–111.

[26] Ambrosio F, Wiktor J, Pasquarello A. Ph-dependent catalytic reaction pathway for water splitting at the $BiVO_4$–Water interface from the band alignment. ACS Energy Lett 2018;3(4):829–34.

[27] Guo Z, Ambrosio F, Pasquarello A. Evaluation of photocatalysts for water splitting through combined analysis of surface coverage and energy-level alignment. ACS Catal 2020;10(22):13186–95.

[28] Zhao Y, Gao J, Bian X, Tang H, Zhang T. From the perspective of experimental practice: High-throughput computational screening in photocatalysis. Green Energy Environ. 2023.

[29] Hu S, Shaner MR, Beardslee JA, Lichterman M, Brunschwig BS, Lewis NS. Amorphous TiO2 coatings stabilize Si, GaAs, and GaP photoanodes for efficient water oxidation. Science 2014;344(6187):1005–9.

[30] Ahmed MG, Kretschmer IE, Kandiel TA, Ahmed AY, Rashwan FA, Bahnemann DW. A facile surface passivation of hematite photoanodes with TiO_2 overlayers for efficient solar water splitting. ACS Appl Mater Interfaces 2015;7(43):24053–62.

[31] Zou Z, Ye J, Arakawa H. Photocatalytic water splitting into H2 and/or O2 under UV and visible light irradiation with a semiconductor photocatalyst. Int J Hydrog Energy 2003;28(6):663–9.

[32] Ambrosio F, Wiktor J, Pasquarello A. Ph-dependent surface chemistry from first principles: Application to the $BiVO_4$(010)–Water interface. ACS Appl Mater Interfaces 2018;10(12):10011–21.

[33] Wen B, Andrade MFC, Liu L-M, Selloni A. Water dissociation at the water–rutile tio_2(110) interface from *ab* initio-based deep neural network simulations. Proc Natl Acad Sci 2023;120(2):e2212250120.

[34] Zhu J, Zäch M. Nanostructured materials for photocatalytic hydrogen production. Curr Opin Colloid Interface Sci 2009;14(4):260–9.

[35] Ikram M, Rashid M, Haider A, Naz S, Haider J, Raza A, Ansar M, Uddin MK, Ali NM, Ahmed SS, et al. A review of photocatalytic characterization, and environmental cleaning, of metal oxide nanostructured materials. Sustain Mater Technol 2021;30:e00343.

[36] Li Y, Gao C, Long R, Xiong Y. Photocatalyst design based on two-dimensional materials. Mater Today Chem 2019;11:197–216.

[37] Di J, Xia J, Li H, Liu Z. Freestanding atomically-thin two-dimensional materials beyond graphene meeting photocatalysis: Opportunities and challenges. Nano Energy 2017;35:79–91.

[38] Ismael M. Ferrites as solar photocatalytic materials and their activities in solar energy conversion and environmental protection: a review. Sol Energy Mater Sol Cells 2021;219:110786.

[39] Ambrosio F, Wiktor J, De Angelis F, Pasquarello A. Origin of low electron–hole recombination rate in metal halide perovskites. Energy Environ Sci 2018;11:101.

[40] Dagnall KA, Foley BJ, Cuthriell SA, Alpert MR, Deng X, Chen AZ, Sun Z, Gupta MC, Xiao K, Lee S-H. Relationship between the nature of monovalent cations and charge recombination in metal halide perovskites. ACS Appl Energy Mater 2020;3:1298.

[41] Brenner TM, Egger DA, Kronik L, Hodes G, Cahen D. Hybrid organic–norganic perovskites: low-cost semiconductors with intriguing charge-transport properties. Nat Rev Mater 2016;1:15007.

[42] Ponseca CS, Savenije TJ, Abdellah M, Zheng K, Yartsev A, Pascher T, Harlang T, Chabera P, Pullerits T, Stepanov A. Organometal halide perovskite solar cell materials rationalized: Ultrafast charge generation, high and microsecond-long balanced mobilities, and slow recombination. J Am Chem Soc 2014;136:5189.

[43] Kojima A, Teshima K, Shirai Y, Miyasaka T. Organometal halide perovskites as visible-light sensitizers for photovoltaic cells. J Am Chem Soc 2009;131:6050.

[44] Burschka J, Pellet N, Moon S-J, Humphry-Baker R, Gao P, Nazeeruddin MK, Grätzel M. Sequential deposition as a route to high-performance perovskite-sensitized solar cells. Nature 2013;499:316.

[45] Stranks SD, Eperon GE, Grancini G, Menelaou C, Alcocer MJP, Leijtens T, Herz LM, Petrozza A, Snaith HJ. Electron-hole diffusion lengths exceeding 1 micrometer in an organometal trihalide perovskite absorber. Science 2013;342:341.

[46] Meggiolaro D, Ambrosio F, Mosconi E, Mahata A, De Angelis F. Polarons in metal halide perovskites. Adv Energy Mater 2020;10:1902748.

[47] Motti SG, Meggiolaro D, Martani S, Sorrentino R, Barker AJ, De Angelis F, Petrozza A. Defect activity in metal-halide perovskites. Adv Mater 2019;31:1901183.

[48] Kim J, Lee S-H, Lee JH, Hong K-H. The role of intrinsic defects in methylammonium lead iodide perovskite. J Phys Chem Lett 2014;5:1312.

[49] Chu W, Zheng Q, Prezhdo OV, Zhao J, Saidi WA. Low-frequency lattice phonons in halide perovskites explain high defect tolerance toward electron-hole recombination. Sci Adv 2020;6:eaaw7453.

[50] Filip MR, Eperon GE, Snaith HJ, Giustino F. Steric engineering of metal-halide perovskites with tunable optical band gaps. Nature Commun 2014;5:5757.

[51] Huang H, Pradhan B, Hofkens J, Roeffaers MBJ, Steele JA. Solar-driven metal halide perovskite photocatalysis: Design, stability, and performance. ACS Energy Lett 2020;5:1107.

[52] Bisquert J, Juarez-Perez EJ. The causes of degradation of perovskite solar cells. J Phys Chem Lett 2019;10:5889.

[53] Zheng C, Rubel O. Unraveling the water degradation mechanism of $CH_3NH_3pbi_3$. J Phys Chem Lett 2019;123:19385.

[54] Mosconi E, Azpiroz JM, De Angelis F. Ab initio molecular dynamics simulations of methylammonium lead iodide perovskite degradation by water. Chem Mater 2015;27:4885.

[55] Leguy A, Hu Y, Campoy-Quiles M, Alonso MI, Weber OJ, Azarhoosh P, van Schilfgaarde M, Weller MT, Bein T, Nelson J. The reversible hydration of $CH_3NH_3pbi_3$ in films, single crystals and solar cells. Chem Mater 2015;27:3397.

[56] Giustino F, Snaith HJ. Toward lead-free perovskite solar cells. ACS Energy Lett 2016;1(6):1233–40.

[57] Noel NK, Stranks SD, Abate A, Wehrenfennig C, Guarnera S, Haghighirad A-A, Sadhanala A, Eperon GE, Pathak SK, Johnston MB. Lead-free organic-inorganic tin halide perovskites for photovoltaic applications. Energy Environ Sci 2014;7:3061.

[58] Hao F, Stoumpos CC, Cao DH, Chang RPH, Kanatzidis MG. Lead-free solid-state organic–inorganic halide perovskite solar cells. Nat Photon 2014;8:489.

[59] Ricciarelli D, Meggiolaro D, Ambrosio F, De Angelis F. Instability of tin iodide perovskites: Bulk p-doping versus surface tin oxidation. ACS Energy Lett 2020;5(9):2787–95.

[60] Meggiolaro D, Ricciarelli D, Alasmari AA, Alasmary FAS, De Angelis F. Tin versus lead redox chemistry modulates charge trapping and self-doping in tin/lead iodide perovskites. J Phys Chem Lett 2020;11:3546.

[61] Dalpian GM, Liu Q, Stoumpos CC, Douvalis AP, Balasubramanian M, Kanatzidis MG, Zunger A. Changes in charge density vs changes in formal oxidation states: The case of Sn halide perovskites and their ordered vacancy analogues. Phys Rev Mater 2017;1:025401.

[62] Bowman AR, Klug MT, Doherty TAS, Farrar MD, Senanayak SP, Wenger B, Divitini G, Booker EP, Andaji-Garmaroudi Z, Macpherson S. Microsecond carrier lifetimes, controlled p-doping, and enhanced air stability in low-bandgap metal halide perovskites. ACS Energy Lett 2019;4:2301.

[63] Yoo JJ, Seo G, Chua MR, Park TG, Lu Y, Rotermund F, Kim Y-K, Moon CS, Jeon NJ, Correa-Baena J-P. Efficient perovskite solar cells via improved carrier management. Nature 2021;590:587.

[64] Ambrosio F, Mosconi E, Alasmari AA, Alasmary FA, Meggiolaro D, De Angelis F. Formation of color centers in lead iodide perovskites: Self-trapping and defects in the bulk and surfaces. Chem Mater 2020;32(16):6916–24.

[65] Wang J, Liu J, Du Z, Li Z. Recent advances in metal halide perovskite photocatalysts: Properties, synthesis and applications. J Energy Chem 2021;54:770–85.

[66] Chen Z-Y, Huang N-Y, Xu Q. Metal halide perovskite materials in photocatalysis: Design strategies and applications. Coord Chem Rev 2023;481:215031.

[67] Armenise V, Colella S, Fracassi F, Listorti A. Lead-free metal halide perovskites for hydrogen evolution from aqueous solutions. Nanomater 2021;11:433.

[68] Romani L, Speltini A, Dibenedetto CN, Listorti A, Ambrosio F, Mosconi E, Simbula A, Saba M, Profumo A, Quadrelli P, et al. Experimental strategy and mechanistic view to boost the photocatalytic activity of Cs3Bi2Br9 lead-free perovskite derivative by g-c3n4 composite engineering. Adv Funct Mater 2021;31(46):2104428.

[69] Romani L, Speltini A, Ambrosio F, Mosconi E, Profumo A, Marelli M, Margadonna S, Milella A, Fracassi F, Listorti A, De Angelis F, Malavasi L. Water-stable DMASnBr3 lead-free perovskite for effective solar-driven photocatalysis. Angew Chem Int Edn 2021;60(7):3611–8.

[70] Tang Y, Mak CH, Jia G, Cheng K-C, Kai J-J, Hsieh C-W, Meng F, Niu W, Li F-F, Shen H-H, Zhu X, Chen HM, Hsu H-Y. Lead-free hybrid perovskite photocatalysts: surface engineering, charge-carrier behaviors, and solar-driven applications. J Mater Chem A 2022;10:12296–316.

[71] Romani L, Speltini A, Chiara R, Morana M, Coccia C, Tedesco C, Armenise V, Colella S, Milella A, Listorti A, Profumo A, Ambrosio F, Mosconi E, Pau R, Pitzalis F, Simbula A, Ricciarelli D, Saba M, Medina-Llamas M, De Angelis F, Malavasi L. Air- and water-stable and photocatalytically active germanium-based 2D perovskites by organic spacer engineering. Cell Rep Phys Sci 2023;4(1):101214.

[72] Chen S, Yin H, Liu P, Wang Y, Zhao H. Stabilization and performance enhancement strategies for halide perovskite photocatalysts. Adv Mater 2023;35(6):2203836.

[73] Pisanu A, Speltini A, Quadrelli P, Drera G, Sangaletti L, Malavasi L. Enhanced air-stability of sn-based hybrid perovskites induced by dimethylammonium (DMA): synthesis, characterization, aging and hydrogen photogeneration of the $MA_{1-x}DMA_xSnBr_3$ system. J Mater Chem C 2019;7:7020.

[74] Speltini A, Romani L, Dondi D, Malavasi L, Profumo A. Carbon nitride-perovskite composites: Evaluation and optimization of photocatalytic hydrogen evolution in saccharides aqueous solution. Catalysts 2020;10(11).

[75] Ouhbi H, Ambrosio F, De Angelis F, Wiktor J. Strong electron localization in tin halide perovskites. J Phys Chem Lett 2021;12(22):5339–43.

[76] Ricciarelli D, Kaiser W, Mosconi E, Wiktor J, Ashraf MW, Malavasi L, Ambrosio F, De Angelis F. Reaction mechanism of photocatalytic hydrogen production at water/tin halide perovskite interfaces. ACS Energy Lett 2022;7(4):1308–15.

[77] DuBose JT, Kamat PV. Efficacy of perovskite photocatalysis: Challenges to overcome. ACS Energy Lett 2022;7(6):1994–2011.

[78] Kaiser W, Ricciarelli D, Mosconi E, Alothman AA, Ambrosio F, De Angelis F. Stability of tin- versus lead-halide perovskites: Ab initio molecular dynamics simulations of perovskite/water interfaces. J Phys Chem Lett 2022;13(10):2321–9.

[79] VandeVondele J, Krack M, Mohamed F, Parrinello M, Chassaing T, Hutter J. Quickstep: Fast and accurate density functional calculations using a mixed Gaussian and plane waves approach. Comput Phys Comm 2005;167(2):103–28.

[80] Nosé S. A unified formulation of the constant temperature molecular dynamics methods. J Chem Phys 1984;81(1):511–9.

[81] Hoover WG. Canonical dynamics: Equilibrium phase-space distributions. Phys Rev A 1985;31:1695–7.

[82] Ambrosio F, Miceli G, Pasquarello A. Redox levels in aqueous solution: Effect of van der waals interactions and hybrid functionals. J Chem Phys 2015;143(24):244508.

[83] Vydrov OA, Van Voorhis T. Nonlocal van der Waals density functional: The simpler the better. J Chem Phys 2010;133(24):244103.

[84] Sabatini R, Gorni T, de Gironcoli S. Nonlocal van der Waals density functional made simple and efficient. Phys Rev B 2013;87:041108.

[85] Goedecker S, Teter M, Hutter J. Separable dual-space Gaussian pseudopotentials. Phys Rev B 1996;54:1703–10.

[86] VandeVondele J, Hutter J. Gaussian basis sets for accurate calculations on molecular systems in gas and condensed phases. J Chem Phys 2007;127(11):114105.

[87] Miceli G, Chen W, Reshetnyak I, Pasquarello A. Nonempirical hybrid functionals for band gaps and polaronic distortions in solids. Phys Rev B 2018;97:121112.

[88] Brawand NP, Govoni M, Vörös M, Galli G. Performance and self-consistency of the generalized dielectric dependent hybrid functional. J Chem Theory Comput 2017;13(7):3318–25.

[89] Bischoff T, Reshetnyak I, Pasquarello A. Adjustable potential probes for band-gap predictions of extended systems through nonempirical hybrid functionals. Phys Rev B 2019;99:201114.

[90] Bischoff T, Wiktor J, Chen W, Pasquarello A. Nonempirical hybrid functionals for band gaps of inorganic metal-halide perovskites. Phys Rev Mater 2019;3:123802.

[91] Perdew JP, Burke K, Ernzerhof M. Generalized gradient approximation made simple. Phys Rev Lett 1996;77:3865–8.

[92] Adamo C, Barone V. Toward reliable density functional methods without adjustable parameters: The PBE0 model. J Chem Phys 1999;110(13):6158–70.

[93] Guidon M, Hutter J, VandeVondele J. Robust periodic Hartree-Fock exchange for large-scale simulations using Gaussian basis sets. J Chem Theory Comput 2009;5(11):3010–21.

[94] Guidon M, Hutter J, VandeVondele J. Auxiliary density matrix methods for Hartree-Fock exchange calculations. J Chem Theory Comput 2010;6(8):2348–64.

[95] Komsa H-P, Rantala TT, Pasquarello A. Finite-size supercell correction schemes for charged defect calculations. Phys Rev B 2012;86:045112.

[96] Todorova M, Neugebauer J. Extending the concept of defect chemistry from semiconductor physics to electrochemistry. Phys Rev A 2014;1:014001.

[97] Di Liberto G, Maleki F, Pacchioni G. Ph dependence of MgO, TiO2, and γAl_2O_3 surface chemistry from first principles. J Phys Chem C 2022;126(24):10216–23.

[98] King G, Warshel A. Investigation of the free energy functions for electron transfer reactions. J Chem Phys 1990;93(12):8682–92.

[99] Cheng J, Liu X, VandeVondele J, Sulpizi M, Sprik M. Redox potentials and acidity constants from density functional theory based molecular dynamics. Acc Chem Res 2014;47(12):3522–9.

[100] Kharche N, Muckerman JT, Hybertsen MS. First-principles approach to calculating energy level alignment at aqueous semiconductor interfaces. Phys Rev Lett 2014;113:176802.

[101] Komsa H-P, Broqvist P, Pasquarello A. Alignment of defect levels and band edges through hybrid functionals: Effect of screening in the exchange term. Phys Rev B 2010;81:205118.

[102] Ambrosio F, Guo Z, Pasquarello A. Absolute energy levels of liquid water. J Phys Chem Lett 2018;9(12):3212–6.

[103] Greeley J, Jaramillo TF, Bonde J, Chorkendorff I, Nø rskov JK. Computational high-throughput screening of electrocatalytic materials for hydrogen evolution. Nature Mater 2006;5(11):909–13.

[104] Zhang L, Jaroniec M. Fundamentals of adsorption for photocatalysis. In: Interface science and technology, Vol. 31, Elsevier; 2020, p. 39–62.

[105] Marzari N, Mostofi AA, Yates JR, Souza I, Vanderbilt D. Maximally localized Wannier functions: Theory and applications. Rev Modern Phys 2012;84(4):1419.

[106] Ambrosio F, Wiktor J. Strong hole trapping due to oxygen dimers in $BiVO_4$: Effect on the water oxidation reaction. J Phys Chem Lett 2019;10(22):7113–8.

[107] Cheng J, VandeVondele J, Sprik M. Identifying trapped electronic holes at the aqueous tio_2 interface. J Phys Chem C 2014;118(10):5437–44.

[108] Gono P, Wiktor J, Ambrosio F, Pasquarello A. Surface polarons reducing overpotentials in the oxygen evolution reaction. ACS Catal 2018;8(7):5847–51.

[109] Gerosa M, Bottani C, Di Valentin C, Onida G, Pacchioni G. Accuracy of dielectric-dependent hybrid functionals in the prediction of optoelectronic properties of metal oxide semiconductors: A comprehensive comparison with many-body GW and experiments. J Phys: Condens Matter 2017;30(4):044003.

[110] Naveen Kumar TR, Karthik P, Neppolian B. Polaron and bipolaron induced charge carrier transportation for enhanced photocatalytic H_2 production. Nanoscale 2020;12:14213.

[111] Zhang L, Chu W, Zhao C, Zheng Q, Prezhdo OV, Zhao J. Dynamics of photoexcited small polarons in transition-metal oxides. J Phys Chem Lett 2021;12:2191.

[112] Pastor E, Park J-S, Steier L, Kim S, Grätzel M, Durrant JR, Walsh A, Bakulin AA. In situ observation of picosecond polaron self-localisation in α-Fe_2O_3 photoelectrochemical cells. Nature Commun 2019;10:3962.

[113] Wang W, Favaro M, Chen E, Trotochaud L, Bluhm H, Choi K-S, van de Krol R, Starr DE, Galli G. Influence of excess charge on water adsorption on the $BiVO_4$(010) surface. J Am Chem Soc 2022;144(37):17173–85.

[114] Wiktor J, Ambrosio F, Pasquarello A. Role of polarons in water splitting: The case of $BiVO_4$. ACS Energy Lett 2018;3(7):1693–7.
[115] de Chialvo M, Chialvo A. Hydrogen evolution reaction: Analysis of the volmer-heyrovsky-tafel mechanism with a generalized adsorption model. J Electroanal Chem 1994;372(1):209–23.
[116] Cheng J, Sprik M. Alignment of electronic energy levels at electrochemical interfaces. Phys Chem Chem Phys 2012;14:11245–67.
[117] Wen X, Fan X-T, Jin X, Cheng J. Band alignment of 2D material–water interfaces. J Phys Chem C 2023;127(8):4132–43.
[118] Ping Y, Sundararaman R, Goddard III WA. Solvation effects on the band edge positions of photocatalysts from first principles. Phys Chem Chem Phys 2015;17:30499–509.
[119] Hörmann NG, Guo Z, Ambrosio F, Andreussi O, Pasquarello A, Marzari N. Absolute band alignment at semiconductor-water interfaces using explicit and implicit descriptions for liquid water. Npj Comput Mater 2019;5(1):100.
[120] Gao YQ, Georgievskii Y, Marcus RA. On the theory of electron transfer reactions at semiconductor electrode/liquid interfaces. J Chem Phys 2000;112(7):3358–69.